MASTER THESIS

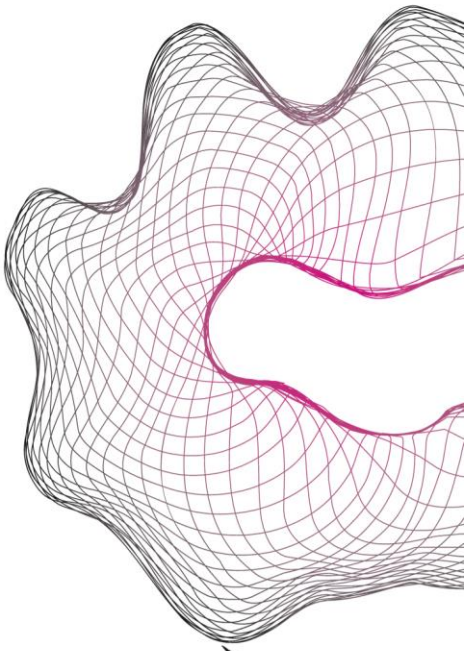

TOWARDS WEARABLE ELECTROMYOGRAPHY BY SENSOR REDUCTION FOR PERSONALIZED MUSCULOSKELETAL TRUNK MODELS IN COMPRESSION FORCE ESTIMATION DURING LIFTING – AN INVERSE SYNERGY-BASED APPROACH

Jan Willem A. Rook

FACULTY OF ENGINEERING TECHNOLOGY
DEPARTMENT OF BIOMECHANICAL ENGINEERING

EXAMINATION COMMITTEE
PROF.DR.IR. M. SARTORI
DR.IR. M.I. REFAI
DR.IR. K. NIZAMIS

UNIVERSITY OF TWENTE.

APRIL 2024

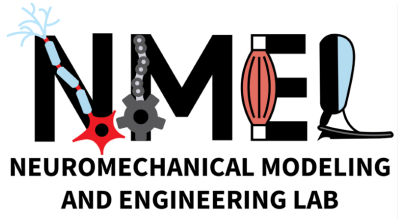
NMEL
NEUROMECHANICAL MODELING
AND ENGINEERING LAB


ROBOTICS CENTRE


TECHMED
CENTRE

CONTENTS

ACRONYMS

BT bilateral twist lift
BW body weight
EMG electromyography
EMS electromyography-driven musculoskeletal model
ID inverse dynamics
IK inverse kinematics
IMU inertial measurement unit
LBP low back pain
MTU muscle-tendon unit
MVC maximum voluntary contraction
MVE minimum variance estimation
NMF non-negative matrix factorization
R^2 coefficient of determination
RMSE root mean squared errors
SNR signal-to-noise ratio
SQ squat lift
ST stoop lift
UT unilateral twist lift
VAF variance accounted for

Towards Wearable Electromyography by Sensor Reduction for Personalized Musculoskeletal Trunk Models in Compression Force Estimation during Lifting – An Inverse Synergy-Based Approach

Jan Willem A. Rook[1], Mohamed Irfan Mohamed Refai*[1], Kostas Nizamis[2] and Massimo Sartori[1]

***Abstract*— Low back pain (LBP) due to occupational lifting is prevalent. Tracking of mechanical loading of the lumbosacral joint is important for risk assessment and employs exoskeleton control. Wearable electromyography-driven musculoskeletal models (EMSs) of the trunk enable this. However, their practical feasibility is hampered due to the large number (12) of electromyography (EMG) sensors involved. Current EMG sensor reduction methods are tailored to specific use cases, which makes translation difficult. We propose in this study a generic sensor reduction method that identifies the minimum number of sensors needed, locates optimal sensor placement, and estimates unmeasured EMG signals based on muscle synergies. These are used to drive a trunk-EMS to estimate lumbosacral joint moments and compression forces. We evaluated this method for 12 participants performing different box lifting tasks (squat, stoop, unilateral twist, and bilateral twist) with various weights (0 kg, 7.5 kg, and 15 kg). Results show that two synergies could explain 90% measured muscle activities for all lifting tasks. Building upon this, two sensors were used to reconstruct the EMG of four unmeasured channels (median RMSE range: 0.02 to 0.04 relative to MVC, median R^2: 0.65 and 0.83). Using a reduced sensor model as input for a trunk-EMS, we compared the resulting lumbosacral joint moments and compression forces against those obtained with a full-sensor setup. Our findings indicate that we successfully reduced the sensor count from 12 to two without significant loss in accuracy for lumbosacral joint moments (median Δ RMSE $\leq$ 0.04 Nm/kg, median Δ R^2 $\leq$ 0.05) and achieved high accuracy in comparing both models for compression force estimation (median RMSE $\leq$ 0.21 $\times$ BW, median R^2 $\geq$ 0.91) across all conditions. This reduction in sensors substantially reduces preparation time and improves the usability of the trunk-EMS.**

I. INTRODUCTION

In 2020, the prevalence of low back pain (LBP) worldwide exceeded half a billion cases, with 22% of years lived with disability attributing to occupational factors [1]. Workers who perform occupational tasks such as trunk flexion, rotation, and lifting have an increased risk of injuries [2]–[4]. These injuries result from increased mechanical stress on structures such as intervertebral disks, facet joints, and surrounding tissues, leading to LBP [5]. Compressive spine forces are a predictor for LBP [6]. These forces are generally highest in the caudal end of the lumbar spine [7]. Commonly, lumbosacral joint moments are used as a suitable proxy for assessing compressive spine forces [8]–[12].

Ambulatory biomechanical risk assessment in occupational settings requires a wearable tool to estimate lumbosacral joint moments and compressive forces. Direct measurement of compression loads on lumbar disks in vivo is invasive [13], [14]. Alternatively, non-invasive modeling approaches can be used. Inverse dynamics (ID) is the gold standard for estimating joint moments [10]. However, ID requires specialized equipment, such as motion-capture cameras and force plates, which are only available in laboratory settings [9], [10]. Additionally, modeling the contribution of muscles to joint moments and compression forces involves addressing muscle redundancy [14]–[16]. Since muscle activation is not measured, static optimization-driven models are needed to estimate muscle forces based on cost functions [17]. Consequently, these models lack a physiological basis for estimating subject-specific muscle forces [14]. Regression-based approaches, on the other hand, address this limitation by estimating lumbosacral joint moments using wearable electromyography (EMG) sensors [10], [12], [18], [19]. However, they do not rely directly on musculoskeletal modeling principles. Passive muscle forces are therefore not taken into account. Consequently, compression forces cannot be estimated, since their magnitude is directly related to back muscle-tendon forces [8].

Electromyography-driven musculoskeletal models (EMSs) estimate muscle forces from subject-specific muscle activity and joint angles [16], [20]. Including muscle forces based on measured muscle activity allows for considering muscle co-contraction effects in estimating lumbosacral joint moments [15]. To estimate lumbosacral joint moments and compression forces during lifting, we previously developed an EMS of the trunk [8]. Here muscle activations are derived from measured EMG and transformed non-linearly to muscle force along with information on joint position [15]. This model shows a strong correlation compared to reference moments obtained through ID (root mean squared errors (RMSE): 0.21–0.38 Nm/kg, coefficient of determination (R^2) mean range: 0.88-0.94). The EMS was further validated for estimations of compressive forces [21]. The EMS uses data from wearable sensors [21]. This enables ambulatory biomechanical risk assessment in occupational settings [11], [14], [22] and contributes to the control of trunk exoskeletons [21].

*This work was supported by the European Union's Horizon 2020 Research and Innovation Programme under Grant Agreement No. 871237 (SOPHIA), and Horizon 2024 Research and Innovation Programme (Grant Agreement No. 101120408; SWAG).

[1]Department of Biomechanical Engineering, University of Twente, Enschede, The Netherlands

[2]Systems Engineering and Multidisciplinary Design group, University of Twente, Enschede, The Netherlands

Unfortunately, the current implementation of EMSs is hindered due to the use of numerous sensors. For instance, our previous setup uses 12 EMG sensors and eight inertial measurement unit (IMU) sensors for muscle activity and joint angle estimation, respectively [8]. This complexity, specifically for EMG sensors [23], leads to the need for specialized expertise, extended preparation time, and user discomfort [19]. To enhance the usability we need EMG sensor reduction to obtain a minimal and robust sensor setup that is easy to apply and calibrate [10].

Several EMG sensor reduction methods are described in the literature, and all utilize a synergy-based approach [24]–[28]. Synergy-based approaches reduce data into a latent low-dimensional representation. These describe how the human central nervous system coordinates the activation of muscles during specific tasks [29]. Synergy analysis involves decomposing EMG signals from collaborating muscles into a low-dimensional set of time-independent synergy vectors, and time-dependent synergy excitations. Matrix decomposition methods, such as non-negative matrix factorization, can extract the synergies from measured EMG data [30]. Muscle activity measured by surface EMG during trunk movement is highly redundant [31]–[33]. This means that the number of synergies is fewer than the total muscles involved. Hence, a synergy-based approach could serve as an effective strategy for sensor reduction during lifting tasks.

Many of the current synergy-based sensor reduction approaches are tailored to their specific use case. Examples are EMG estimates for muscles that cannot be measured using surface EMG [24]–[26], or minimum variance estimation (MVE) models to estimate unmeasured joint angles and EMG from a task-oriented prior distribution [27], [28]. Tailoring makes these approaches less generalizable and potentially overcomplicates the models. We refer to our trunk-EMS, where the surface EMG of all important muscles is accessible. Also, EMG estimation based on task-oriented prior distributions has drawbacks. Defining a prior distribution poses challenges, and increases model complexity. Additionally, MVE models only estimate muscle activity based on movement and do not incorporate muscle tone and regulation of joint stiffness [27]. This reduces the validity of the prior distribution.

The goal is to develop an inverse synergy-based sensor reduction model and assess its applicability across various lifting tasks and weights. The first subgoal is to clarify the underlying principles of the inverse synergy-based model. The second subgoal is to evaluate the calibration of the inverse synergy-based model. These include the minimum number of sensors and subject-specific optimal sensor locations. The third subgoal is to evaluate the reconstruction accuracy of unmeasured EMG sensors and assess their impact on lumbosacral joint moments and compression forces. This involves comparing the reconstructed EMG channels with their reference values and examining the outcomes of a full-sensor EMS compared to a reduced-sensor EMS.

II. THEORETICAL FOUNDATIONS

In this section, we explain how synergies can be used to achieve sensor reduction. We first introduce the inverse synergy-based method, followed by an explanation of how to identify muscle synergies and select optimal sensor locations.

A. Inverse synergy-based sensor reduction

We can use the dimensionality reduction from matrix decomposition to estimate unmeasured EMG activations. The decomposition of an EMG matrix $\mathbf{V}$ of m muscles and n samples into a linear combination of k time-independent synergy vectors $\mathbf{W}$ and scaled time-varying synergy excitations $\mathbf{H}$ is given by

$$\mathbf{V}_{(m\times n)} \approx \mathbf{W}_{(m\times k)} \times \mathbf{H}_{(k\times n)} \tag{1}$$

with $k < m$. The dimensionality reduction, given by the difference between m and k, enables us to describe the EMG signal of m muscles through k synergies. We can now fully determine the system using minimally k sensors instead of m sensors, and since $k < m$ this reduces the number of sensors. However, there are several requirements. First of all, we have to be able to obtain $\mathbf{W}$ from a calibration procedure where we measure all m muscles. This $\mathbf{W}$ matrix needs to be valid for all movements for which we want to estimate the EMG. In the literature, this approach is referred to as a spatial synergy model [34] when fixed synergy vectors are used. Second, the time-dependent nature of synergy excitations in $\mathbf{H}$ is influenced by movement technique and execution speed. We therefore have to approximate synergy excitations, indicated

Nomenclature

ε	Error
f_c	Cut-off frequency
$\mathbf{F}_C$	Compression force
F_{GRF}	Ground reaction force
F_H	Hand force
$\mathbf{H}$	Synergy excitations matrix
$\mathbf{H}^*$	Approximated synergy excitations
k	Number of synergies
l_{MTU}	Muscle-tendon unit length
m	Number of muscles
$\mathbf{M}_{FE}$	Lumbosacral flexion-extension moment
n	Number of samples
$\mathbf{p}$	Array of sensors
r	Moment arm
θ	Full-body joint angles
$\mathbf{V}$	Full EMG matrix
$\mathbf{V}^*$	Submatrix of EMG matrix
$\mathbf{W}$	Full synergy vectors matrix
$\mathbf{W}^*$	Submatrix of synergy vectors
$\mathbf{W}^{*\dagger}$	Pseudo-inverse of $\mathbf{W}^*$
x_{marker}	Full-body marker data

by $\mathbf{H}^*$, from $\mathbf{V}$ and $\mathbf{W}$ for each sample. However, instead of using the full $\mathbf{V}$ and $\mathbf{W}$ matrices, we could use submatrices, where we select at least k and at most $m-1$ rows. The selected rows of the submatrices indicated as scalars in the array $\mathbf{p}$, correspond to the sensor locations of the measured muscles. So the submatrices are given by

$$\mathbf{V}^* = \mathbf{V}_{(\mathbf{p},k)} \tag{2a}$$

$$\mathbf{W}^* = \mathbf{W}_{(\mathbf{p},k)} \tag{2b}$$

The strategy to determine how many sensors to select (corresponding to the total number of components in $\mathbf{p}$, given by $|\mathbf{p}|$) and their optimal location (corresponding to the entries of $\mathbf{p}$) will be explained in II-B and II-C. By rewriting eq. (1) into a least-squares problem, we approximate $\mathbf{H}^*$ from $\mathbf{V}^*$ and $\mathbf{W}^*$

$$\mathbf{H}^* = \underbrace{(\mathbf{W}^{*T}\mathbf{W}^*)^{-1}\mathbf{W}^{*T}}_{\mathbf{W}^{*\dagger}}\mathbf{V}^* \tag{3}$$

Here, $\mathbf{W}^{*\dagger}$ is the pseudo-inverse of $\mathbf{W}^*$. In case $k = |\mathbf{p}|$ and $\mathbf{W}^*$ is invertible, the pseudo-inverse is equal to $(\mathbf{W}^*)^{-1}$. To reconstruct the estimated EMG matrix, $\mathbf{V}_{est}$, we can perform

$$\mathbf{V}_{est} = \mathbf{W} \times \mathbf{H}^* = \mathbf{W} \times \mathbf{W}^{*\dagger} \times \mathbf{V}^* \tag{4}$$

B. Synergy identification

Muscle synergies can be identified by matrix decomposition algorithms that group muscles that move together into synergies, as shown in eq. (1). Because there are many ways to create synergy vectors to decide how much each muscle contributes to a synergy, we can find many different solutions for breaking down the same EMG matrix [34]. Applying constraints like non-negativity, sparse distribution, or mutual orthogonality to the synergy vectors helps produce a distinct set. However, results differ between algorithms since each algorithm uses different constraints to find an optimal solution. Many studies use non-negative matrix factorization (NMF) to find $\mathbf{W}$ and $\mathbf{H}$ [26], [31]–[35]. NMF minimizes the Frobenius norm residuals and applies non-negativity constraints to $\mathbf{W}$ and $\mathbf{H}$ given by:

$$\min_{\mathbf{W},\mathbf{H}} \|\mathbf{V} - \mathbf{W}\mathbf{H}\|_F^2 \quad \text{subject to} \quad \mathbf{W} \geq 0, \mathbf{H} \geq 0 \tag{5}$$

When using the identified synergies for sensor reduction, an additional constraint, related to the step described in equation 3, becomes necessary to consider. As described, we use the pseudo-inverse of $\mathbf{W}^*$ in eq. 3. To perform this operation, $\mathbf{W}^*$ has to be well-conditioned. The condition number of a matrix indicates how sensitive matrix inversion is to errors in the input [36]. So, an error $\varepsilon_{\mathbf{H}^*}$ in $\mathbf{H}^*$ will correspondingly result in an error $\varepsilon_{\mathbf{V}_{est}}$ in $\mathbf{V}_{est}$, according to:

$$\mathbf{W}^* \times (\mathbf{H}^* + \varepsilon_{\mathbf{H}^*}) = \mathbf{V}_{est} + \varepsilon_{\mathbf{V}_{est}} \tag{6}$$

A matrix is considered well-conditioned if its condition number falls within the range of 1 (the optimal value) to 100. However, if the condition number ranges between 10^6 and 10^{16}, it is considered ill-conditioned [37]. So, when choosing the decomposition algorithm, the algorithm of choice must provide a well-conditioned $\mathbf{W}^*$.

The primary parameter to determine in a matrix decomposition algorithm is the number of synergies k. This parameter reflects the dimensionality of EMG data and represents the minimum number of vectors required to explain most of the data variance. Typically, a variance accounted for (VAF) threshold, often set between 0.8 and 0.95, is used to determine k [34]. Once this threshold is established, the decomposition results can be evaluated by comparing the VAF of $\mathbf{W} \times \mathbf{H}$ to $\mathbf{V}$ against the threshold. Additionally, k is crucial for determining the minimum number of sensors required to estimate the synergy excitations. Specifically, at least k sensors are needed to approximate the k synergy excitations. However, it is possible to use more sensors, a strategy known as oversampled sensor placement [36].

C. Optimal sensor locations

Conditioning also plays a significant role in determining the optimal sensor locations. Selecting the optimal sensor locations boils down to identifying the set of muscles that best estimate all included synergies. When examining the synergy vectors in matrix $\mathbf{W}$, the goal is to incorporate the muscles with the highest values for individual synergies. Therefore, to determine the optimal sensor locations (corresponding to the rows in $\mathbf{W}$) we seek a submatrix whose volume is maximized for the individual synergies (corresponding to the columns in $\mathbf{W}$). Directly optimizing this problem involves evaluating $\binom{|\mathbf{p}|}{k}$ possible sensor configurations, which becomes too difficult to solve computationally for large $\mathbf{W}$ [36].

An effective solution to this problem, as described by Manohar et al. [36], involves using QR-factorization of $\mathbf{W}^T$ if $k = |\mathbf{p}|$, and QR-factorization of $\mathbf{W}\mathbf{W}^T$ in case of oversampled sensor placement ($k < |\mathbf{p}|$) to find a greedy solution for the best sensor locations. In essence, the QR-factorization algorithm decomposes $\mathbf{W}^T$ into a unitary matrix $\mathbf{Q}$ and an upper triangular matrix $\mathbf{R}$, such that $\mathbf{W}^T = \mathbf{Q}\mathbf{R}$. QR column pivoting increases the size of the submatrix made from the pivot columns. This expansion of the submatrix volume concerning the synergies aligns with our objective. Therefore, QR-factorization with column pivoting provides an efficient method to select the optimal sensor combination.

III. METHODS

A. Participants

Participant inclusion criteria were: (1) older than 18 years, (2) height between 1.55 and 1.95 meters, (3) weight less than 95 kg. 12 healthy (7 men, 5 women, age: 29.7± 12.5 years, weight: 71.7±9.6 kg, height: 177.9±8.3 cm) participants were included. None suffered from back injuries, and all gave written informed consent. Ethical approval was obtained from the Natural Sciences and Engineering Sciences Ethics Committee of the University of Twente (application number: 230447).

B. Experimental Protocol

The experimental protocol was designed to resemble common occupational lifting tasks regarding lifting techniques, box dimensions, and weights [38], [39]. All participants lifted a box ($w \times d \times h = 40 \times 30 \times 22$ cm, empty weight = 1.2 kg) using two symmetric techniques: squat lift (SQ) and stoop lift (ST), and two asymmetric techniques: unilateral twist lift (UT) and bilateral twist lift (BT). An overview is shown in fig. 1.

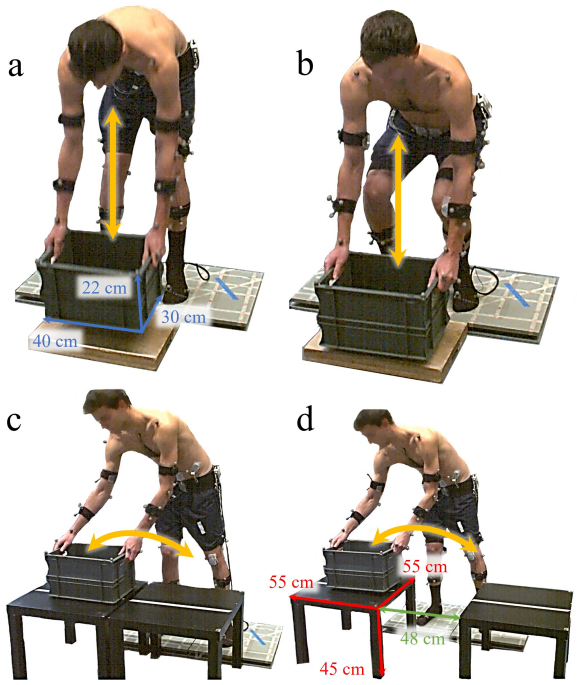

Fig. 1. Overview of the four different box lifting techniques: Stoop lift (a), Squat lift (b), Unilateral Twist lift (c), Bilateral Twist lift (d). Yellow arrows indicate box directions during lifting, blue arrows indicate box dimensions, red arrows indicate table dimensions and the green arrow indicates the distance between the two tables during a bilateral twist.

The SQ and ST techniques involved lifting the box in front of the participant from a wooden platform ($h = 6$ cm), to place the initial box position at the same ground level as the participant standing on the force plates. Once the participant stood upright, the box was placed back in its original position using the same lifting technique in reverse order. Unlike the SQ and ST, the UT and BT techniques involved moving the box from a table ($w \times d \times h = 55 \times 55 \times 45$ cm). For UT (fig. 1c), the table was positioned in front of the participant, while for BT (fig. 1d), it was diagonally to the left. The box was then transferred to another identical table diagonally positioned to the right in front of the participant. After standing straight, the participant returned the box to the starting table. These actions include one UT or BT movement. Participants maintained a steady pace by performing all liftings in sync with a 30 beats per minute metronome. For each lifting technique, three different weight conditions were considered. The box contained either no additional weight (0 kg), 7.5 or 15 kg[3]. One trial consisted of either six (SQ and ST) or three (UT and BT) repetitions. So the total number of liftings per participant was $(6+3)(2 \times 3) = 54$. Between trials, there was a brief recovery period of approximately 20 seconds to prevent muscle fatigue onset. The trials were grouped for symmetric and asymmetric techniques. The order of symmetric or asymmetric trials and the sequence within these trials were randomized.

C. Data collection and measurement setup

Surface EMG with bipolar electrodes (Delsys Bagnoli, Delsys Incorporated, Boston, MA) and ground reaction forces (GRF) from dual-force plates (AMTI, MA) were recorded at 2048 Hz. A 12-camera optical motion capture system (Qualisys Medical AB, Gothenburg, Sweden) was used to record full-body and box kinematics at 128 Hz.

Fig. 2 shows the EMG placement on the body for all recorded muscles. This included six dorsal muscles: *Longissimus Thoracis pars Thoracis* (LTpT), *Longissimus Thoracis pars Lumborum* (LTpL), and *Iliocostalis Lumborum* (IL) (fig. 2a) and six ventral muscles: *External Oblique* (EO), *Rectus Abdominis* (RA), and *Internal Oblique* (IO) (fig. 2b). A description of the EMG placement is given in table I. The 3D trajectories of 61 spherical reflective markers were recorded for full-body inverse kinematics (IK). The markers were placed on bony landmarks and body segments (triplet clusters). Their locations are listed in appendix A. Box kinematics were obtained using four markers on each top corner of the box.

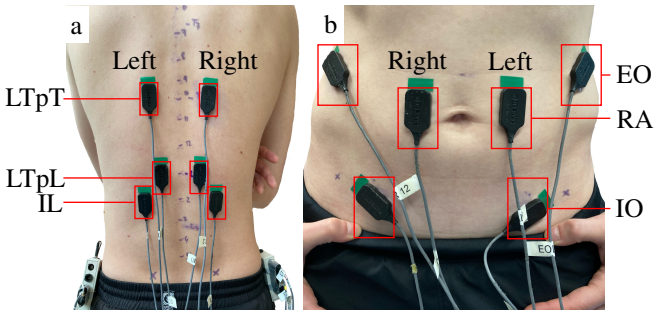

Fig. 2. EMG placement for the six dorsal muscles (a): *Longissimus Thoracis pars Thoracis* (LTpT), *Longissimus Thoracis pars Lumborum* (LTpL), *Iliocostalis Lumborum* (IL) and the six ventral muscles (b): *External Oblique* (EO), *Rectus Abdominis* (RA), and *Internal Oblique* (IO).

TABLE I
DESCRIPTION OF THE EMG PLACEMENT FOR ALL RECORDED MUSCLES.

		EMG placement
Ventral muscles	LTpT	4 cm lateral from T10
	LTpL	3 cm lateral from L1
	IL	6 cm lateral from L2
Dorsal muscles	EO	On the middle of the midaxillary line
	RA	3 cm lateral from midline at umbilicus level
	IO	Just superior to the inguinal ligament

[3]From hereon, these conditions are used to indicate the weight conditions.

D. Data processing

MATLAB (2022a, The Mathworks, Natick, MA) was used for data processing and further analysis. For data processing, we used the same pipeline as previously described in [8]. Linear EMG envelopes were obtained by consecutively bandpass filtering (f_c : 30 – 300 Hz), full-wave rectifying, and low-pass filtering (f_c : 6 Hz) of the recorded EMG signals using a second-order zero-lag Butterworth filter. EMG linear envelopes were normalized using data from maximum voluntary contraction (MVC) recordings with a moving window of 0.05 seconds[4]. The MVC values for ventral muscles were obtained during upper trunk flexion, while those for dorsal muscles were acquired during upper trunk extension. MVC trials were performed as described in [23], [40], [41]. GRF and marker trajectories were low-pass filtered (f_c : 6 Hz) using a second-order zero-lag Butterworth filter. After filtering, all recorded signals were resampled at 50 Hz. After pre-processing, data from each lifting cycle were resampled to 1001 time points, representing the entire lifting phase from start (0%, just before the participant began reaching for the box, standing straight) to end (100%, just after the participant had returned to the initial standing position, standing straight).

E. Input EMG signals for full- and reduced-sensor model

As mentioned in section III-C, EMG data was collected from six ventral and six dorsal muscles. These 12 muscles were used as input for the full-sensor model. Nevertheless, it has been frequently observed that ventral muscles exhibit low amplitude signals [8], [13] and the effect of antagonistic co-contraction has been reported to be minor during lifting [42]. Therefore we hypothesized that these six muscles could be considered unmeasured. Consequently, synergy analysis was conducted by including the six dorsal muscles while excluding the ventral ones. This approach offers advantages. Excluding these channels enables a further reduction in the number of required synergies.

[4]From hereon, EMG refers to these normalized EMG linear envelopes, unless stated otherwise.

F. Inverse synergy-based sensor reduction

We explain in this section how we applied our inverse synergy-based sensor reduction method. Fig. 3 shows the flowchart, which encompasses data splitting (step 1), calibration (steps 2 and 3, highlighted in orange), and reconstruction (step 4, highlighted in blue). Appendix B shows the MATLAB code.

1) Data Splitting: Initially, trials were categorized randomly into a calibration dataset $\mathbf{V}_{cal}$ or a validation dataset $\mathbf{V}_{val}$. For each movement-weight combination, two out of six trials were used in the calibration dataset for SQ and ST, while one out of three trials was used for UT and BT. All trials selected for the calibration dataset were concatenated (resulting in length N_{cat}) in $\mathbf{V}_{cal}$.

2) Synergy extraction from calibration data: We determined in the first calibration step the time-invariant synergy vector matrix $\mathbf{W}$ by decomposition. We applied NMF to $\mathbf{V}_{cal}$ with the number of synergies k ranging from one to six, using MATLAB's `NNMF` function. The identified $\mathbf{W}$ was then saved and later used for obtaining $\mathbf{V}_{est}$ across all combinations of movement and weight.

3) Optimal sensors from calibration data: The second calibration step involved selecting the optimal sensor locations. The minimum number of sensors was determined by identifying the minimum k that was needed to explain VAF ≥ 0.90, also known as the threshold method [30]. How we calculated the variability will be further explained in section III-I. We matched the number of sensors $|\mathbf{p}|$ with k to achieve maximal sensor reduction (so $k = |\mathbf{p}|$). We used QR factorization with column pivoting of $\mathbf{W}^T$ to find optimal sensors. We found $\mathbf{W}^*$ by selecting the rows in $\mathbf{W}$ corresponding to these optimal sensors.

4) EMG reconstruction of the validation data: We approximated $\mathbf{H}^*$ for each timestep n based on $\mathbf{W}^*$ and $\mathbf{V}^*$ from validation data. We reconstructed unmeasured EMG channels in $\mathbf{V}_{est}$ by multiplying $\mathbf{W}$ by $\mathbf{H}^*$.

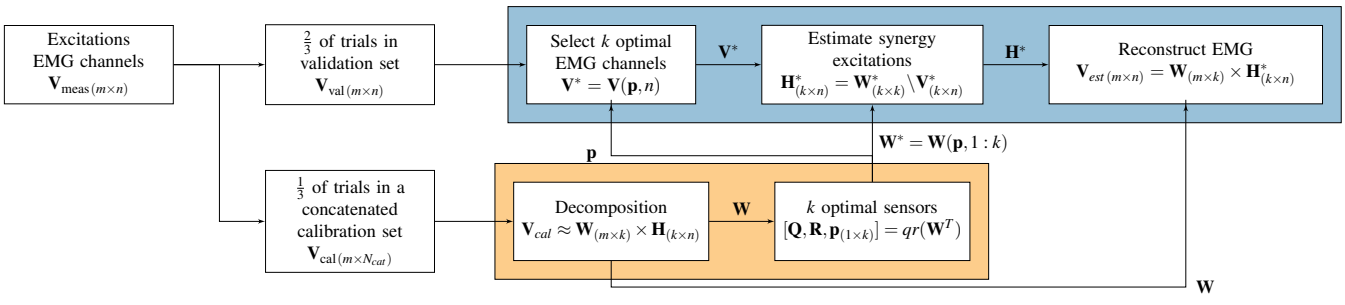

Fig. 3. This flowchart outlines the inverse synergy-based workflow. The orange box shows the calibration, while the blue box indicates the reconstruction. **Step 1:** Splitting the EMG linear envelopes of m muscles ($\mathbf{V}_{meas}$) into a validation set ($\mathbf{V}_{val}$) and a calibration set ($\mathbf{V}_{cal}$). For each participant, $\mathbf{V}_{cal}$ consists of EMG signals of all m muscles, and selected calibration trials (with concatenated length N_{cat}). **Step 2:** The $\mathbf{V}_{cal}$ is the input of the NMF algorithm to obtain a time-invariant synergy vector matrix $\mathbf{W}_{(m\times k)}$. **Step 3:** From $\mathbf{W}_{(m\times k)}$, $k = |\mathbf{p}|$ optimal sensor locations (indicated by $\mathbf{p}_{(1\times k)}$) are chosen using a QR factorization algorithm, and a reduced synergy vector matrix ($\mathbf{W}^*_{(k\times k)}$) is created from their corresponding entries in $\mathbf{W}_{(m\times k)}$. Only these k sensors from $\mathbf{V}_{val}$ are treated as measured (indicated by $\mathbf{V}(\mathbf{p}, n)$). The time-variant excitation matrix $\mathbf{H}^*_{(k\times n)}$ is estimated using a least-squares approximation. **Step 4:** $\mathbf{V}_{est}$ is reconstructed from $\mathbf{H}^*_{(k\times n)}$ and $\mathbf{W}_{(m\times k)}$ from calibration.

G. Dynamics modeling

Dynamics modeling was performed in OpenSim 4.3. The OpenSim lifting full-body geometry model by Beaucage-Gauvreau et al. [43] was linearly scaled to match each participant's anthropometry using bony landmark markers. The full-body model consisted of 238 Hill-type muscle-tendon units (MTUs) that model the properties of the lumbar, thoracic, and abdominal muscles. For the box dynamics, an OpenSim box model (with the aforementioned dimensions and weight) was used to simulate box movements. Both models were used to perform IK and ID to estimate lumbosacral flexion-extension moments ($\mathbf{M}_{FE}$). IK of the full-body model resulted in full-body joint angles (θ), MTU-lengths (l_{MTU}), and moment arms (r). IK and ID of the box provided moments and translational forces. These acted only during box-lifting on the hands. Upon detecting box movement from marker data, we applied resulting forces to the mid-position between the second and fifth knuckles in the full-body model. Finally, joint moments were obtained by employing ID on the full-body model, using joint angles along with ground reaction forces (F_{GRF}) and hand forces (F_H).

H. EMG-driven musculoskeletal modeling

For EMG-driven musculoskeletal modeling we used our previously developed trunk-EMS [8]. This model was created using the Calibrated EMG-informed Neuromusculoskeletal toolbox (CEINMS) [20]. Figure 4 shows how signals from both dynamics modeling and EMG-driven musculoskeletal modeling are linked in this study.

1) Calibration phase: For each participant, a subject-specific EMS was created (fig 4, red box). Maximal isometric force, tendon slack length, and optimal fiber length were calibrated for each of the 238 modeled MTUs using 12-sensor EMG data, l_{MTU}, r, and reference full-body ID (fig 4, blue box). The calibration procedure was similar to [8], and involved selecting one random lifting trial for each movement and weight for calibration. This process tuned the aforementioned MTU parameters to establish a calibrated EMS for each participant.

2) Execution phase: Following calibration, we estimated $\mathbf{M}_{FE}$ and compression forces ($\mathbf{F}_C$) for trials not included in calibration, only with EMG as input, along with l_{MTU} and r obtained from lumbosacral joint angles. The full-EMS used EMG from all 12 measured sensors ($\mathbf{V}_{full}$). The reduced-EMS used EMG from six dorsal sensors ($\mathbf{V}_{reduced}$), and ventral muscles provided only passive forces (as previously explained in III-E). The matching between EMG channels and MTUs in the full-body model is detailed in table II for both full- and reduced-EMS. Musculoskeletal geometry parameters l_{MTU} and r were obtained from lumbosacral joint angles using full-body IK.

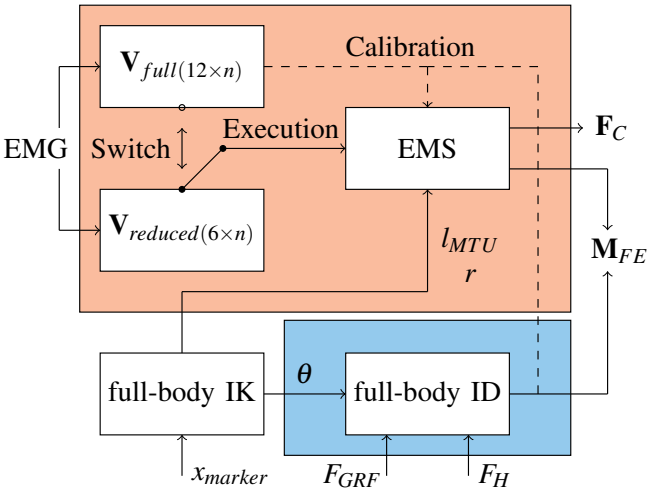

Fig. 4. Overview of the signal flow for obtaining lumbosacral flexion-extension moments ($\mathbf{M}_{FE}$) and compression forces ($\mathbf{F}_C$). The red box represents the EMS created from the CEINMS toolbox, and the blue box represents ID. Calibration of the EMS was performed based on full-sensor measured EMG trials ($\mathbf{V}_{meas(12\times n)}$) and associated $\mathbf{M}_{FE}$ from ID. During model execution, $\mathbf{V}_{full(12\times n)}$ and reduced-sensor EMG from dorsal muscles ($\mathbf{V}_{reduced(6\times n)}$) were used. These were inputs for the same subject-specific calibrated EMS in the execution phase, indicated by the switch. Subject-specific parameters like MTU lengths (l_{MTU}), and moment arms (r) were obtained from full-body IK based on marker data (x_{marker}). IK joint angles (θ) were used for ID, combined with all acting forces on the body, including ground reaction forces (F_{GRF}) and hand forces (F_H). From ID, the reference $\mathbf{M}_{FE}$ was calculated. $\mathbf{M}_{FE}$ from both full- and reduced-EMS were compared to the gold standard ID to evaluate the calibration of the EMS.

TABLE II

MAPPING BETWEEN EMG CHANNELS AND MTU GROUPS OF THE FULL-BODY MODEL (NUMBER OF MTUS WITHIN EACH GROUP IN PARENTHESIS). UNMEASURED MUSCLES WERE NOT ASSIGNED (N.A.) AND ONLY PASSIVE FORCE WAS CONSIDERED.

MTU group (full-body model)	**EMG channel (full-EMS)**	**EMG channel (reduced-EMS)**
Multifidus (50) Longissimus thoracis pars lumborum (10)	LTpL	LTpL
Iliocostalis lumborum pars lumborum (8)	IL	IL
Longissimus thoracis pars thoracis (42) Iliocostalis lumborum pars thoracis (16)	LTpT	LTpT
Rectus abdominis (2) External oblique (12) Internal oblique (12)	RA EO IO	N.A. (passive)
Psoas major (22) Quadratus lumborum (36) Latissimus dorsi (28)	N.A. (passive)	N.A. (passive)
Σ 238 MTUs	12	6 (k measured, $m-k$ reconstructed)

I. Data analysis

1) Determination of the minimum number of synergies: To find the minimum number of synergies (k) from the calibration set ($\mathbf{V}_{cal}$) that corresponds to the number of columns of $\mathbf{W}_{(m\times k)}$ from NMF, we used the VAF, defined as follows:

$$VAF = 1 - \frac{RSS}{TSS} = 1 - \frac{\sum(\mathbf{V}_{cal} - \mathbf{W}_{(m\times k)} \times \mathbf{H}_{(k\times n)})^2}{\sum(\mathbf{V}_{cal})^2} \quad (7)$$

Here RSS and TSS are the residual and total sum of squares, respectively. The optimal number of decomposition columns in $\mathbf{W}_{(m\times k)}$, corresponding to the optimal number of sensors, was found when the median VAF exceeds 0.90 for a specific k. VAF values range from 0 (no explained variability) to 1 (perfect fit).

2) Model evaluation: For model evaluation, we compared reconstructed EMG channels in $\mathbf{V}_{est}$ (indicated by $\mathbf{V}_{rec}$) to their measured values in $\mathbf{V}_{val}$ (indicated as reference values). We used RMSE to evaluate the average magnitude of prediction errors for n samples:

$$RMSE = \sqrt{\frac{\sum(\mathbf{V}_{val} - \mathbf{V}_{rec})^2}{n}} \quad (8)$$

Interpreting RMSE is straightforward: a lower value indicates better model performance, and 0 indicates a perfect fit. For normalized EMG values, the worst RMSE score is 1.

We used the coefficient of determination (R^2) to evaluate the extent to which the variance of the reconstructed EMG ($\mathbf{V}_{rec}$) explains the variance of the reference ($\mathbf{V}_{val}$):

$$R^2 = 1 - \frac{RSS}{TSS} = 1 - \frac{\sum(\mathbf{V}_{val} - \mathbf{V}_{rec})^2}{\sum(\mathbf{V}_{val} - \bar{\mathbf{V}}_{val})^2} \quad (9)$$

Note that while the definitions of VAF and R^2 are similar, the TSS for VAF is concerning zero, whereas for R^2, it is related to the mean ($\bar{\mathbf{V}}_{val}$) [30]. Unlike VAF, R^2 can be negative, indicating poorer performance than a constant predictor using the mean (resulting in R^2 = 0). The maximum value for R^2 is 1.

RMSE and R^2 were also used to evaluate the performance of the full- and reduced-EMS. For lumbosacral flexion-extension moments, $\mathbf{V}_{val}$ was substituted for $\mathbf{M}_{FE}$ from ID, and $\mathbf{V}_{rec}$ was substituted for either the full- or reduced-EMS. For compression forces, $\mathbf{V}_{val}$ was substituted for $\mathbf{F}_C$ from full-EMS and $\mathbf{V}_{rec}$ was substituted for $\mathbf{F}_C$ from reduced-EMS.

3) Statistical analysis: We tested for normality using Shapiro-Wilk tests to compare RMSE and R^2 values between the paired observations of the full- and reduced-EMS to ID, considering $\mathbf{M}_{FE}$. The majority demonstrated non-normal distributions. Therefore, we further analyzed differences using non-parametric Wilcoxon signed-rank tests. Here, the null hypothesis was that the median differences between the paired observations were zero. For $p \leq 0.05$ this hypothesis was rejected.

IV. RESULTS

We first determined the minimum number of synergies (IV-A) and identified optimal sensor locations for each subject (IV-B). Then, we compared the reconstructed EMG data from the reduced-EMS to the full-EMS to assess reconstruction accuracy (IV-C) and detect outliers (IV-D). We compared the lumbosacral joint moments of both models against the gold standard ID to evaluate the calibration of the EMS (IV-E). Finally, we compared the compression forces of both models (IV-F).

A. Muscle synergies

Table III shows that when the number of synergies increased from one to six, the median VAF of the reconstructed calibration data also increased, while the interquartile range (IQR) decreased. For $k \geq 2$, we see a median VAF ≥ 0.90. Therefore we used subject-specific synergy matrices for $k = 2$ (i.e. ($\mathbf{W}_{(6\times 2)}$ and $\mathbf{W}^*_{(2\times 2)}$) for EMG reconstruction.

TABLE III
RECONSTRUCTION VAF OF THE NMF DECOMPOSED CALIBRATION DATA OF ALL SUBJECTS. FOR ≥ 2 SYNERGIES, THE MEDIAN VAF ≥ 0.90.

Number of synergies	VAF Median (IQR)
1	0.85 (0.10)
2	0.90 (0.10)
3	0.95 (0.08)
4	0.98 (0.07)
5	1.00 (0.02)
6	1.00 (0.00)

B. Sensor locations and EMG estimation

Table IV shows where sensors were placed on all participants using the QR factorization algorithm. The LTpL muscles were chosen most frequently (16 times). Upon examining sides, the left side was favored more than the right. Further analysis shows that all participants except one (subject 9) had a bilateral sensor placement. This single exception had two left sensors, which accounts for the difference between the totals for the left and right sides. See also appendix C.

TABLE IV
THE OPTIMAL SENSOR LOCATIONS FOR ALL PARTICIPANTS, PER MUSCLE (COLUMNS) AND SIDE (ROWS). TOTALS ARE PROVIDED IN ITALICS.

Sensor location	LTpT	LTpL	IL	Σ_{Side}
Left	2	8	3	*13*
Right	3	8	0	*11*
Σ_{muscle}	*5*	*16*	*3*	*24*

Fig. 5 illustrates results from a representative participant. Reconstruction using the inverse synergy-based approach is demonstrated across several weights, including 0 kg (a), 7.5 kg (b), and 15 kg (c) for an SQ, and several lifting

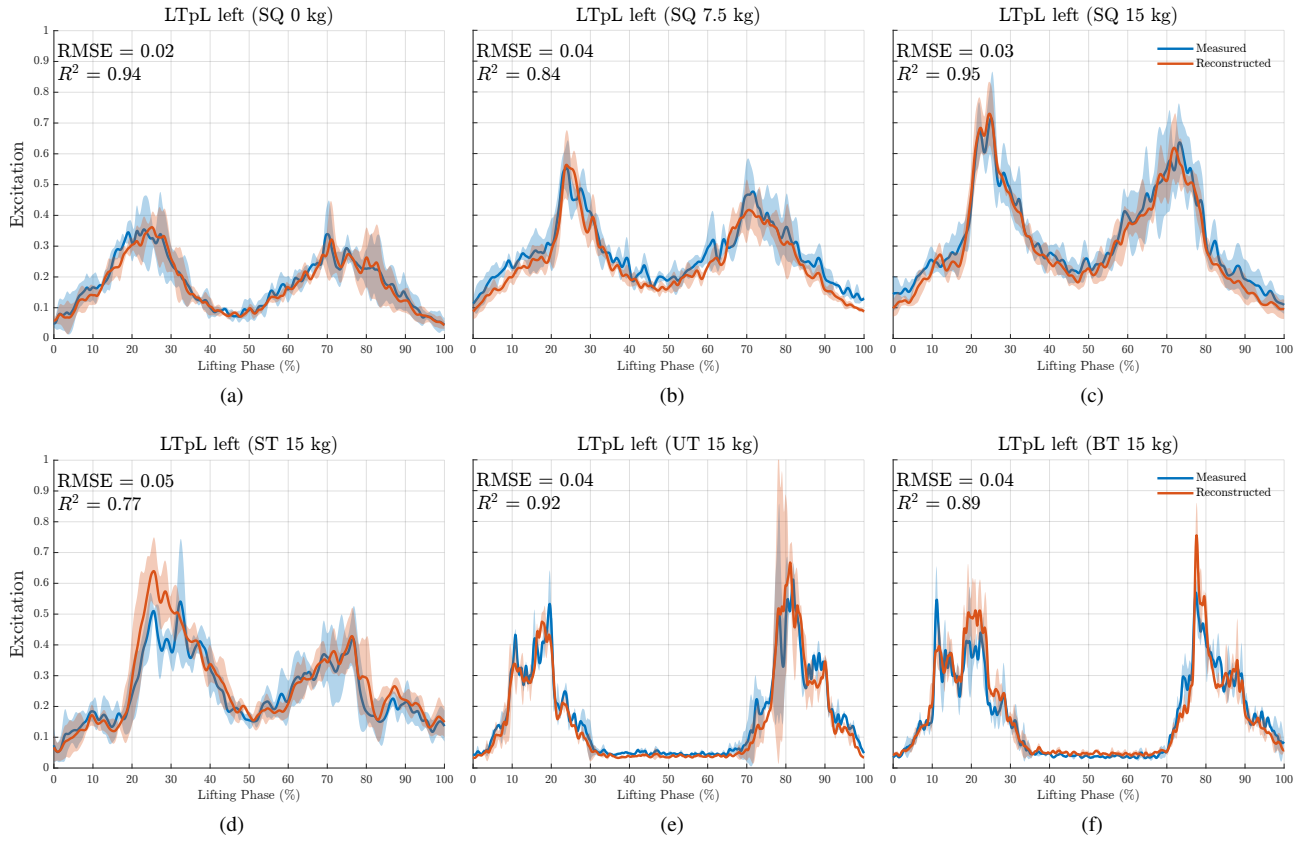

Fig. 5. Measured and estimated EMG from 1 participant (subject 5) for the left LTpL muscle (sensor locations are LTpT right and IL left). Plots a-c show the EMG during SQ liftings with increasing weight, respectively 0 kg (a), 7.5 kg (b), and 15 kg (c). Plots c-d show the EMG for lifting 15 kg using different lifting techniques, respectively SQ (c), ST (d), UT (e), and BT (f)

techniques, including an ST (d), UT (e), and BT (f) with 15 kg weight. The sensor locations for this participant were LTpT right and IL left. The model scaled EMG based on weight, and the temporal alignment of peaks in the reconstructed signal corresponded to those in the reference signal.

C. Reconstruction accuracy

Table V shows median RMSE and R^2 for reconstructed EMG for all movement and weight conditions. We observe median RMSE values ranging between 0.02 and 0.04 relative to MVC. Generally, the RMSE increased with higher weights. The median R^2 values ranged between 0.65 and 0.83. Similarly, we observe an increased R^2 with higher weights.

D. Outliers

Fig. 6 shows the joint distribution of RMSE and R^2 values. Some outliers had $R^2 < 0$, especially for 0 kg and 7.5 kg. Additionally, we see more instances of $0 \leq R^2 \leq 0.5$ for 0 kg compared to 7.5 kg and 15 kg. In contrast, RMSE outliers were related to higher weights. To determine the presence of peaks in the measured EMG signal, we looked if the EMG values exceeded a threshold of 5% (of the MVC) above the mean EMG signal value for at least 10% of the lifting phase. Trials failing to surpass this threshold were indicated with a cross. Many outliers for $R^2 < 0$ did not contain EMG peaks above this threshold. Outliers were not excluded to assess their impact on joint moments and compression forces.

TABLE V

RMSE AND R^2 BETWEEN REFERENCE EMG ($\mathbf{V}_{val}$) AND RECONSTRUCTED EMG ($\mathbf{V}_{rec}$). MEDIAN VALUES (IQR) ACROSS ALL PARTICIPANTS ARE SHOWN.

	EMG*	
	RMSE [-]	R^2 [-]
SQ 0 kg	0.02 (0.01)	0.77 (0.35)
SQ 7.5 kg	0.03 (0.01)	0.82 (0.19)
SQ 15 kg	0.03 (0.02)	0.83 (0.11)
ST 0 kg	0.02 (0.01)	0.77 (0.25)
ST 7.5 kg	0.03 (0.02)	0.76 (0.22)
ST 15 kg	0.04 (0.02)	0.82 (0.18)
UT 0 kg	0.02 (0.01)	0.71 (0.45)
UT 7.5 kg	0.03 (0.01)	0.78 (0.38)
UT 15 kg	0.03 (0.02)	0.83 (0.21)
BT 0 kg	0.02 (0.02)	0.65 (0.35)
BT 7.5 kg	0.03 (0.02)	0.74 (0.34)
BT 15 kg	0.04 (0.02)	0.81 (0.25)

*Reconstructed sensors only

E. Lumbosacral moment estimation

Lumbosacral flexion-extension moments ($\mathbf{M}_{FE}$) were estimated using the 12-sensor full-EMS, and the two-sensor

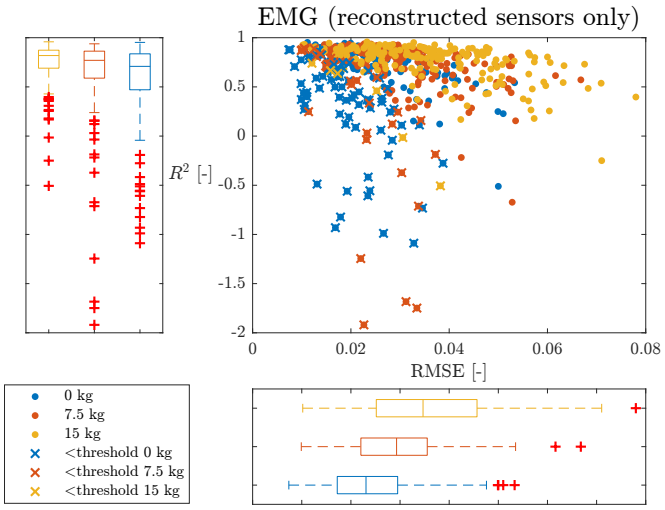

Fig. 6. Boxplots and scatter plot showing the joint distribution of RMSE and R^2 values for reconstructed muscles only (4 muscles × 12 participants × 12 conditions = 576 data points). Crosses in the scatter plot indicate data points for trials where EMG excitation values did not exceed the threshold of 5% (of the MVC) above the mean signal value for at least 10% of the lifting phase.

reduced-EMS. The reference $\mathbf{M}_{FE}$ were obtained from ID.

Table VI shows the median RMSE and R^2 values comparing full- and reduced-EMS to reference ID. Median RMSE values ranged from 0.13 to 0.38 for full-EMS, and from 0.14 to 0.42 for reduced-EMS. The maximal median RMSE difference between both models was 0.04 Nm/kg (SQ 15 kg). Median differences were only significant for UT 7.5 kg, UT 15 kg, and BT 15 kg. Median R^2 values ranged from 0.53 to 0.91 for full-EMS, and from 0.50 to 0.87 for reduced-EMS. Median R^2 differences between full- and reduced-EMS ranged from 0.01 to 0.05. These differences were only significant for UT 15 kg and BT 15 kg.

Fig. 7 shows mean $\mathbf{M}_{FE}$ for full-EMS, reduced-EMS, and ID. Peak $\mathbf{M}_{FE}$ increased with increasing lifted weights for all lifting techniques. The $\mathbf{M}_{FE}$ of full- and reduced-EMS were similar across all lifting tasks, including their standard deviations. Both EMS models showed analogous patterns compared to ID. The most notable differences were observed for 15 kg trials, where both EMSs showed lower $\mathbf{M}_{FE}$ compared to ID. For ST 0 kg, both EMSs showed increased $\mathbf{M}_{FE}$ compared to ID.

F. Compression forces

Table VII shows the median RMSE and R^2 values comparing compression forces ($\mathbf{F}_C$) for full- and reduced-EMS. Median RMSE values ranged from 0.12 to 0.21. Generally, the RMSE increased with higher weights. Median R^2 values ranged between 0.91 and 0.98.

Fig. 8 shows mean $\mathbf{F}_C$ for full- and reduced-EMS normalized to body weight (BW). The $\mathbf{F}_C$ of full- and reduced-EMS were similar across all lifting tasks, including their standard deviations. Mean peak magnitudes during 15 kg lifting were highest for SQ (5.5 × BW), followed by ST (4.7 × BW), BT (4.5 × BW), and UT (4.4 × BW).

TABLE VII

RMSE AND R^2 OF COMPRESSION FORCES ($\mathbf{F}_C$) NORMALIZED TO BODY WEIGHT (BW) BETWEEN FULL-EMS AND REDUCED-EMS. MEDIAN VALUES (IQR) ACROSS ALL PARTICIPANTS ARE SHOWN.

	RMSE [× BW]	R^2 [-]
SQ 0 kg	0.16 (0.12)	0.91 (0.13)
SQ 7.5 kg	0.14 (0.10)	0.97 (0.04)
SQ 15 kg	0.20 (0.14)	0.97 (0.05)
ST 0 kg	0.13 (0.08)	0.95 (0.11)
ST 7.5 kg	0.16 (0.12)	0.95 (0.09)
ST 15 kg	0.21 (0.15)	0.94 (0.06)
UT 0 kg	0.12 (0.09)	0.97 (0.08)
UT 7.5 kg	0.15 (0.11)	0.98 (0.04)
UT 15 kg	0.21 (0.12)	0.97 (0.03)
BT 0 kg	0.12 (0.10)	0.96 (0.07)
BT 7.5 kg	0.16 (0.10)	0.97 (0.03)
BT 15 kg	0.21 (0.12)	0.97 (0.03)

TABLE VI

RMSE AND R^2 FROM THE COMPARISON OF FULL-EMS AND REDUCED-EMS MODELS TO ID CONSIDERING LUMBOSACRAL FLEXION-EXTENSION MOMENTS ($\mathbf{M}_{FE}$). MEDIAN VALUES (IQR) ACROSS ALL PARTICIPANTS ARE SHOWN. ALSO, MEDIAN DIFFERENCES (Δ) AND P-VALUES OF THE COMPARISON BETWEEN THE PAIRED OBSERVATIONS ARE SHOWN.

	RMSE [Nm/kg]				R^2 [-]			
	full-EMS	reduced-EMS	Δ	p-value	full-EMS	reduced-EMS	Δ	p-value
SQ 0 kg	0.18 (0.06)	0.18 (0.08)	0.00	0.569	0.86 (0.12)	0.85 (0.20)	0.01	0.380
SQ 7.5 kg	0.27 (0.11)	0.29 (0.09)	0.02	0.092	0.79 (0.11)	0.77 (0.12)	0.02	0.151
SQ 15 kg	0.38 (0.14)	0.42 (0.13)	0.04	0.339	0.74 (0.16)	0.70 (0.15)	0.04	0.380
ST 0 kg	0.33 (0.14)	0.36 (0.15)	0.03	0.622	0.53 (0.52)	0.50 (0.48)	0.03	0.791
ST 7.5 kg	0.32 (0.10)	0.33 (0.10)	0.01	0.151	0.70 (0.18)	0.68 (0.19)	0.02	0.233
ST 15 kg	0.33 (0.12)	0.36 (0.14)	0.03	0.111	0.74 (0.22)	0.73 (0.23)	0.01	0.092
UT 0 kg	0.13 (0.07)	0.14 (0.08)	0.01	0.339	0.91 (0.09)	0.86 (0.12)	0.05	0.339
UT 7.5 kg	0.21 (0.08)	0.23 (0.07)	0.02	0.034*	0.90 (0.04)	0.87 (0.06)	0.03	0.064
UT 15 kg	0.33 (0.07)	0.35 (0.10)	0.02	0.034*	0.84 (0.06)	0.81 (0.09)	0.03	0.034*
BT 0 kg	0.14 (0.07)	0.15 (0.06)	0.01	0.092	0.90 (0.12)	0.87 (0.12)	0.03	0.151
BT 7.5 kg	0.23 (0.08)	0.24 (0.09)	0.01	0.129	0.88 (0.06)	0.86 (0.07)	0.02	0.233
BT 15 kg	0.36 (0.12)	0.39 (0.15)	0.03	0.027*	0.82 (0.12)	0.80 (0.11)	0.02	0.042*

* significant differences ($p \leq 0.05$) tested with the Wilcoxon signed rank test

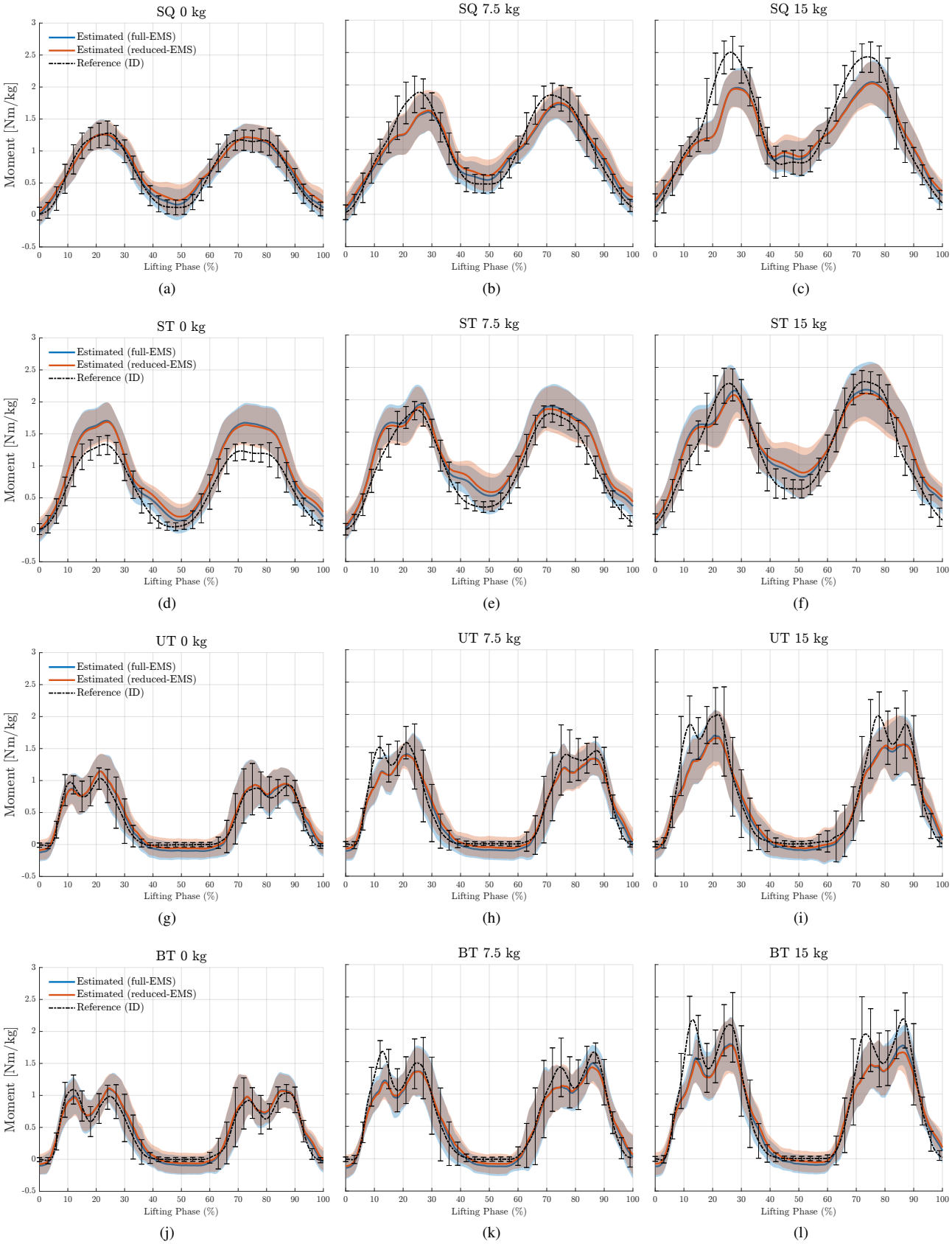

Fig. 7. Mean lumbosacral flexion-extension moments are depicted for full-EMS (blue line), reduced-EMS (orange line), and ID (black dashed line), with standard deviation represented by shaded areas for EMS and bars for ID. Moments were normalized to body weight. Columns represent lifting techniques with the same weight, while rows represent the same lifting techniques with increasing weight from left to right.

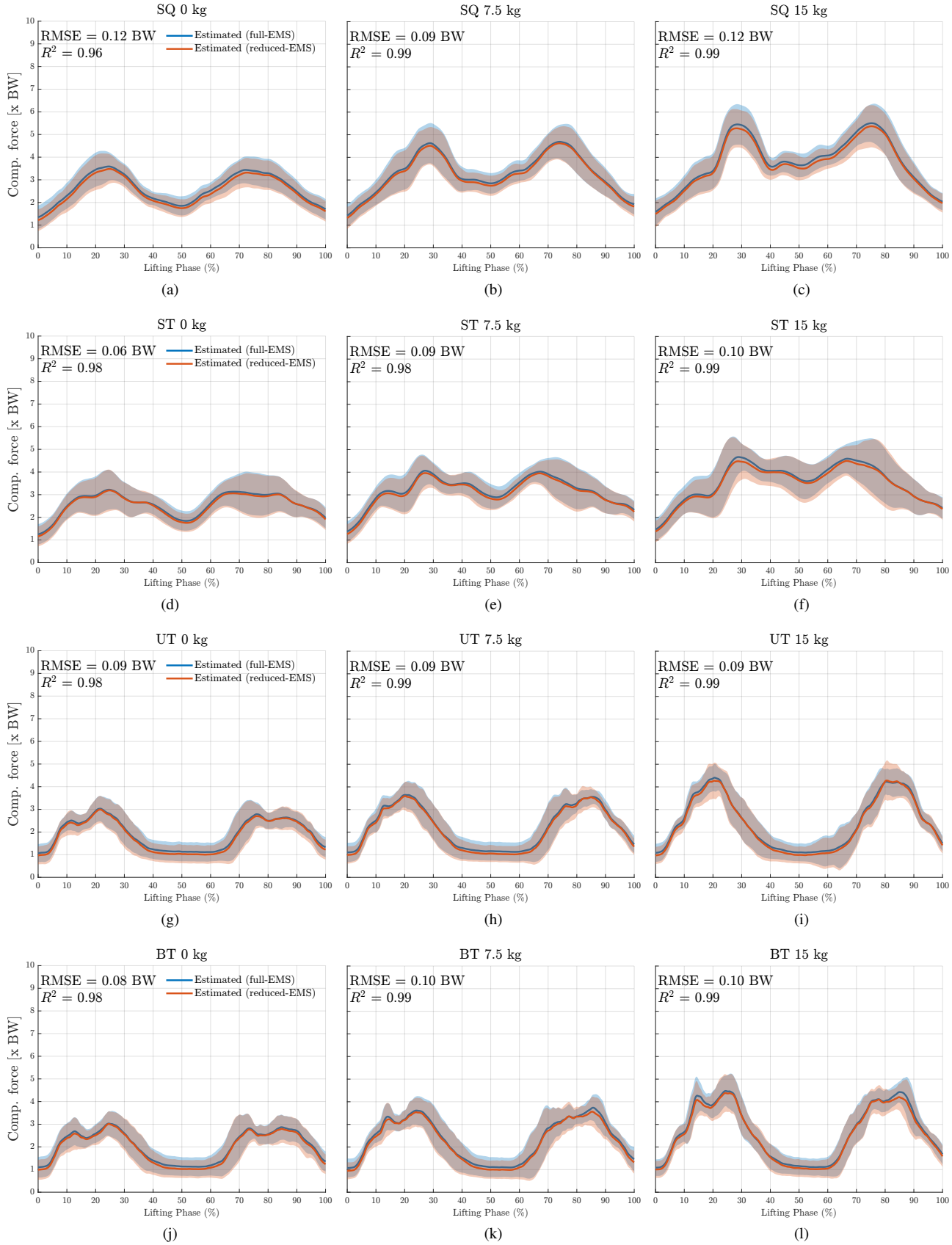

Fig. 8. Mean compression forces are depicted for full-EMS (blue line) and reduced-EMS (orange line) with standard deviation represented by shaded areas. Compression forces were normalized to body weight (BW). Columns represent lifting techniques with the same weight, while rows represent the same lifting techniques with increasing weight from left to right. Also RMSE and R^2 between mean compression forces of full-EMS and reduced-EMS are shown.

V. DISCUSSION

In this study, we present an inverse synergy-based approach for sensor reduction. This method enables the reconstruction of EMG signals from unmeasured muscles by leveraging identified muscle synergies and selecting optimal sensor locations. These EMG signals can be used as input for an EMS to estimate joint moments and compression forces. We assessed the effectiveness of this approach in common occupational lifting tasks regarding symmetric (SQ, ST) and asymmetric (UT, BT) techniques, and different weight conditions (0, 7.5, 15 kg). Two synergies were sufficient to explain 90% VAF. Therefore, two sensors were used for EMG reconstruction of four unmeasured dorsal muscles. The LTpL muscles were optimal sensor locations for most participants. Evaluation of the reconstructed and reference EMG showed median RMSE ranging from 0.02 to 0.04 relative to MVC, and median R^2 between 0.65 and 0.83. Using a reduced sensor model as input for a trunk-EMS, we compared lumbosacral joint moments and compression forces to those obtained with a full-sensor setup. Our results demonstrate that we were able to reduce the number of sensors from 12 to two while maintaining minimal sacrifice in accuracy for lumbosacral joint moments (median Δ RMSE $\leq$ 0.04 Nm/kg, median Δ $R^2 \leq 0.05$) and achieving high accuracy for compression forces (median RMSE $\leq$ 0.21 $\times$ BW, median $R^2 \geq 0.91$) across all conditions. This sensor reduction significantly enhances the usability of the trunk-EMS, as EMG sensor placement in the correct anatomical locations on the skin is a tedious process and hinders the adoption of trunk-EMSs in occupational settings.

A. EMG reconstruction

We used the threshold method for obtaining the optimal number of synergies and found that two synergies gave a median VAF of 0.90. Obtaining the optimal number of synergies is important since too many synergies result in an overdetermined system, which is undesirable as we aim for a minimum sensor approach. Conversely, having too few synergies possibly leads to missing EMG peaks, and will cause errors when used as input for an EMS. Our findings are consistent with Wang et al. [33], who also identified that two muscle synergy groups explain at least 90% VAF. Their study encompassed various movements, including flexion/extension, lateral bending, axial rotation, sitting, and standing. Notably, these movements, except sitting, are relevant to both symmetric and asymmetric box lifting. Sedaghat-Nejad et al. [32] identified a set of four synergies. Differences between their findings and ours could arise from including ventral muscles in their synergy analysis. This may necessitate a greater number of synergies to explain synergy excitation variances. Similar reasons could explain the differences with Tan et al. [31], who identified three synergies but included the biceps brachii and gluteus maximus muscles in their analysis.

We observed that also using one synergy achieves a reasonably good median VAF (0.85). This is due to the similarity in EMG excitation patterns for left- and right-sided dorsal muscles during symmetric lifting movements. However, during asymmetric lifting, EMG peaks may be missed due to expected peaks at different instances of the lifting phase for left and right-sided muscles.

In examining sensor locations, we used QR pivots to maximize the absolute value of the determinant of the reduced synergy vector matrix, $\mathbf{W}^*$. This method aims to increment the volume of $\mathbf{W}^*$ constructed from the pivoted columns of $\mathbf{W}$, preventing an ill-conditioned system. When using two sensors, selecting sensors corresponding to the highest column values in the first and second columns of $\mathbf{W}$ yields the same outcome as employing QR pivots. As the number of sensors increases, choosing the most optimal ones becomes less evident. For example, Bianco et al. [26] explored all combinations of sensors (24,310) to find optimal channels. In these situations, QR pivots provide a simple and effective strategy [36].

QR factorization identified optimal sensor locations on either side of the back. However, this was not the case for one participant, who had two optimal sensors identified on the left side. The reason for this difference is not obvious and must be explored further. Additionally, there was a clear preference for the LTpL as the optimal sensor location. However, we also observed diverse optimal sensor locations among participants. This could be caused by varying EMG scaling based on individual MVC differences. Normalization directly impacts synergy vectors, and this affects their similarities between participants [34]. This could explain the observed diversity in optimal sensor locations since these were chosen based on the synergy vectors.

The results indicate that using two sensors allows for reconstructing the EMG of four unmeasured muscles, with RMSE values ranging from 0.02 for all 0 kg weights to 0.04 for ST 15 kg and BT 15 kg. Overall, we observed low median RMSE errors (all below 5% of MVC) for all lifting techniques and box weights. Median RMSE values increased for increased box weights. This can be explained because lifting heavier weights is characterized by peaks in the EMG excitation signal. Time delays between the reconstructed and reference peaks may cause an increased RMSE and reconstruction errors in peak height.

Median R^2 values range from 0.65 for BT 0 kg to 0.83 for SQ 15 kg and ST 15 kg. However, we observed significant outliers that occasionally fall below zero. These outliers were predominantly associated with median (7.5 kg) and low (0 kg) box weights. Notably, low R^2 values did not exhibit a direct correlation with high RMSE. Baseline differences caused by noise or constant tonic muscle activity may account for these variations, as mentioned by [34]. This could have a large influence on the R^2, since it is sensitive to these errors, as they significantly impact the differences in the mean of the reconstructed and reference signals. An illustration is provided in "Effects of an offset in the EMG signal". Variations in the signal-to-noise ratio (SNR) between reconstructed and measured channels could also contribute. Specifically, if a reconstructed signal from a measured EMG exhibits a high SNR in comparison to a reference signal with a low SNR, it may lead to a low R^2.

Effects of an offset in the EMG signal

An example of an offset effect in the EMG signal is illustrated in Figure 9. Two independent EMG linear envelopes (EMG_1 and EMG_2) were modeled with fictional data using a Gaussian function:

$$f(x) = A \times \exp\left(-\frac{(x-\mu)^2}{2\sigma^2}\right) \tag{10}$$

The third EMG linear envelope, EMG_3, is linearly dependent on both EMG_1 and EMG_2. The functions representing these three EMG signals are given by:

$$EMG_1 = f(x, A = 0.05, \mu = 30, \sigma = 7.5) \tag{11a}$$
$$EMG_2 = f(x, A = 0.06, \mu = 70, \sigma = 5) \tag{11b}$$
$$EMG_3 = 0.8\ EMG_1 + 0.2\ EMG_2 \tag{11c}$$

Figure 9a shows these functions. This data can be treated as training data, and the algorithm outlined in Appendix A can be applied to obtain $\mathbf{W}$, identify the optimal sensors, and use these sensors to reconstruct an EMG signal for one of the unmeasured channels. As expected, the optimal sensor locations correspond to EMG_1 and EMG_2, which are used to estimate EMG_3. However, when a constant offset of 0.02 is added to the EMG_1 channel of the measurement data (figure 9b), we see that this offset directly affects the reconstructed EMG_3 signal. Given that the offset is relatively large compared to the maximum peak height, it significantly influences the R^2 score of the reconstructed EMG_3 relative to the actual signal (RMSE = 0.02, R^2 = -0.78).

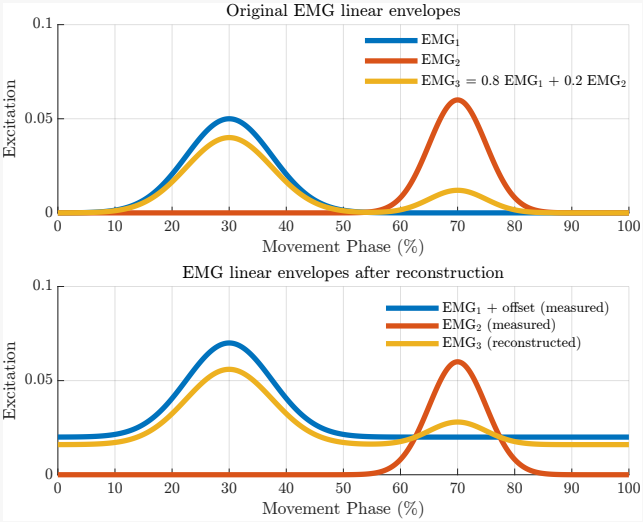

Fig. 9. Example of the effect of an offset in EMG_1 to the reconstructed EMG_3. The comparison of the original EMG_3 and EMG_3 after reconstruction shows an RMSE of 0.02 and an R^2 value of -0.78.

B. Lumbosacral moment estimation

Generally, lumbosacral joint moment differences between full-EMS and reduced-EMS were small. When analyzing the differences (Δ) in RMSE, we observed that all deviations were below 0.05 Nm/kg. Practically, this implies that for a participant with a weight of 75 kg, the RMSE remains below 3.75 Nm. However, some median values between full-EMS and reduced-EMS differed significantly, with full-EMS showing lower median RMSE and higher R^2. An explanation could be that calibration for both EMSs was conducted solely on full EMG data, which included ventral muscles. This decision was made to eliminate the possibility that differences between the full- and reduced-EMS were attributable to distinct calibration models. Considering these small differences, we believe they are outweighed by the benefits of sensor reduction. Reducing the number of EMG sensors from 12 to two significantly enhances the practical usability of an EMS [23].

Comparing our full-EMS results to those obtained by Moya-Esteban et al. [8] we observe differences. While the RMSE ranges appear similar (Moya-Esteban reported a mean range of RMSE between 0.21–0.38 Nm/kg, and we observe median RMSE values between 0.13-0.38 Nm/kg), notable distinctions appear in the ranges for R^2. Moya-Esteban reported a mean range of R^2 between 0.88-0.94, whereas we observe lower median R^2 values between 0.53-0.91, accompanied by larger deviations. There are several explanations for this difference. First, Moya-Esteban did not evaluate the empty box-lifting (0 kg) conditions, which exhibit a low R^2 for ST lifting in this study. Second, variations in optimization settings during EMS calibration could influence the results, along with the choice of tendon model. While Moya-Esteban employed an elastic tendon model, our study used a rigid one.

C. Compression forces

Compression forces are similar between full- and reduced-EMS with high accuracy for compression forces (median RMSE $\leq 0.21\times$ BW, median $R^2 \geq 0.91$) across all conditions. Moya-Esteban et al. [8] reported mean peak compression forces for 15 kg lifts for SQ, ST, and BT (in their study a twist-transfer) of respectively 7.8, 7.5 and 7.7 $\times$ BW. The differences, respectively 2.3, 2.8, and 3.2 $\times$ BW are quite large, and show that our full-EMS underestimates compression forces compared to theirs. A study by Kingma et al. reported peak compression forces closer to our observations. They found for 15 kg SQ and ST mean peak compression forces of respectively 5.3 and 6.2 $\times$ BW [44].

Although the peak compression forces vary, we anticipate no significant impact on the performance of the inverse synergy-based model. Differences are probably caused by calibration and model variations regarding the EMS. However, the inverse synergy-based approach only uses measured

EMG signals and operates independently of the EMS.

D. Limitations

The number of repeated lifting trials was limited, particularly for asymmetrical lifting tasks. This limitation was a result of balancing the inclusion of diverse lifting movements and weights within the constraints of measurement time. Second, we used laboratory equipment to simulate ambulatory sensors. Estimating the joint angle with IMUs instead of marker-based IK could introduce higher errors. However, previous demonstrations of the full-EMS have shown its real-time applicability using IMUs for estimating lumbosacral joint angles [21]. Since differences between the full- and reduced-EMS are small, we also do not expect explicit discrepancies when using IMUs for joint angle estimation.

E. Future work

The next step is to implement the inverse synergy-based approach in a real-time EMS to evaluate the real-time estimation of unmeasured EMGs, lumbosacral joint moments, and compression forces. These can then be used for real-time exoskeleton control and tracking of mechanical loading of the lumbosacral joint for risk assessment of occupational lifting tasks.

REFERENCES

[1] M. L. Ferreira, K. De Luca, L. M. Haile, *et al.*, "Global, regional, and national burden of low back pain, 1990–2020, its attributable risk factors, and projections to 2050: a systematic analysis of the Global Burden of Disease Study 2021," *The Lancet Rheumatology*, vol. 5, no. 6, e316–e329, Jun. 2023, ISSN: 26659913. DOI: 10.1016/S2665-9913(23)00098-X.

[2] W. E. Hoogendoorn, P. M. Bongers, H. C. W. de Vet, *et al.*, "Flexion and Rotation of the Trunk and Lifting at Work Are Risk Factors for Low Back Pain," *Spine*, vol. 25, no. 23, pp. 3087–3092, Dec. 2000, ISSN: 0362-2436. DOI: 10.1097/00007632-200012010-00018. [Online]. Available: http://journals.lww.com/00007632-200012010-00018.

[3] F. Lötters, A. Burdorf, J. Kuiper, and H. Miedema, "Model for the work-relatedness of low-back pain.," *Scandinavian journal of work, environment & health*, vol. 29, no. 6, pp. 431–40, Dec. 2003, ISSN: 0355-3140. DOI: 10.5271/sjweh.749. [Online]. Available: http://www.ncbi.nlm.nih.gov/pubmed/14712849.

[4] P. Coenen, V. Gouttebarge, A. S. A. M. van der Burght, *et al.*, "The effect of lifting during work on low back pain: a health impact assessment based on a meta-analysis," *Occupational and Environmental Medicine*, vol. 71, no. 12, pp. 871–877, Dec. 2014, ISSN: 1351-0711. DOI: 10.1136/oemed-2014-102346. [Online]. Available: https://oem.bmj.com/lookup/doi/10.1136/oemed-2014-102346.

[5] N. N. Knezevic, K. D. Candido, J. W. S. Vlaeyen, J. Van Zundert, and S. P. Cohen, "Low back pain," *The Lancet*, vol. 398, no. 10294, pp. 78–92, Jul. 2021, ISSN: 01406736. DOI: 10.1016/S0140-6736(21)00733-9. [Online]. Available: https://linkinghub.elsevier.com/retrieve/pii/S0140673621007339.

[6] P. Coenen, I. Kingma, C. R. L. Boot, P. M. Bongers, and J. H. van Dieën, "Cumulative mechanical low-back load at work is a determinant of low-back pain.," *Occupational and environmental medicine*, vol. 71, no. 5, pp. 332–7, May 2014, ISSN: 1470-7926. DOI: 10.1136/oemed-2013-101862. [Online]. Available: http://www.ncbi.nlm.nih.gov/pubmed/24676271.

[7] M. von Arx, M. Liechti, L. Connolly, C. Bangerter, M. L. Meier, and S. Schmid, "From Stoop to Squat: A Comprehensive Analysis of Lumbar Loading Among Different Lifting Styles," *Frontiers in Bioengineering and Biotechnology*, vol. 9, Nov. 2021, ISSN: 22964185. DOI: 10.3389/fbioe.2021.769117.

[8] A. Moya-Esteban, H. van der Kooij, and M. Sartori, "Robust estimation of lumbar joint forces in symmetric and asymmetric lifting tasks via large-scale electromyography-driven musculoskeletal models," *Journal of Biomechanics*, vol. 144, p. 111 307, Nov. 2022, ISSN: 00219290. DOI: 10.1016/j.jbiomech.2022.111307. [Online]. Available: https://linkinghub.elsevier.com/retrieve/pii/S0021929022003487.

[9] A. S. Koopman, I. Kingma, G. S. Faber, J. Bornmann, and J. H. van Dieën, "Estimating the L5S1 flexion/extension moment in symmetrical lifting using a simplified ambulatory measurement system," *Journal of Biomechanics*, vol. 70, pp. 242–248, Mar. 2018, ISSN: 18732380. DOI: 10.1016/j.jbiomech.2017.10.001.

[10] S. L. Peters, A. Tabasi, I. Kingma, W. van Dijk, and J. H. van Dieën, "Development of a real time estimation method of L5S1 moments in occupational lifting," *Journal of Biomechanics*, vol. 146, p. 111 417, Jan. 2023, ISSN: 00219290. DOI: 10.1016/j.jbiomech.2022.111417. [Online]. Available: https://linkinghub.elsevier.com/retrieve/pii/S0021929022004584.

[11] C. C. Roossien, C. T. M. Baten, M. W. P. van der Waard, M. F. Reneman, and G. J. Verkerke, "Automatically determining lumbar load during physically demanding work: A validation study," *Sensors*, vol. 21, no. 7, Apr. 2021, ISSN: 14248220. DOI: 10.3390/s21072476.

[12] A. Tabasi, I. Kingma, M. P. de Looze, W. van Dijk, A. S. Koopman, and J. H. van Dieën, "Selecting the appropriate input variables in a regression approach to estimate actively generated muscle moments around L5/S1 for exoskeleton control," *Journal of Biomechanics*, vol. 102, Mar. 2020, ISSN: 18732380. DOI: 10.1016/j.jbiomech.2020.109650.

[13] I. Takahashi, S.-i. Kikuchi, K. Sato, and N. Sato, "Mechanical Load of the Lumbar Spine During Forward Bending Motion of the Trunk–A Biomechanical Study," *Spine*, vol. 31, no. 1, pp. 18–23, Jan. 2006, ISSN: 0362-2436. DOI: 10.1097/01.brs.0000192636.69129.fb. [Online]. Available: http://journals.lww.com/00007632-200601010-00006.

[14] M. Dreischarf, A. Shirazi-Adl, N. Arjmand, A. Rohlmann, and H. Schmidt, "Estimation of loads on human lumbar spine: A review of in vivo and computational model studies," *Journal of Biomechanics*, vol. 49, no. 6, pp. 833–845, Apr. 2016, ISSN: 18732380. DOI: 10.1016/j.jbiomech.2015.12.038.

[15] T. S. Buchanan, D. G. Lloyd, K. Manal, and T. F. Besier, "Estimation of muscle forces and joint moments using a forward-inverse dynamics model.," *Medicine and science in sports and exercise*, vol. 37, no. 11, pp. 1911–6, Nov. 2005, ISSN: 0195-9131. DOI: 10.1249/01.mss.0000176684.24008.6f. [Online]. Available: http://www.ncbi.nlm.nih.gov/pubmed/16286861.

[16] D. G. Lloyd and T. F. Besier, "An EMG-driven musculoskeletal model to estimate muscle forces and knee joint moments in vivo," *Journal of Biomechanics*, vol. 36, no. 6, pp. 765–776, Jun. 2003, ISSN: 00219290. DOI: 10.1016/S0021-9290(03)00010-1.

[17] N. Arjmand, A. Plamondon, A. Shirazi-Adl, C. Larivière, and M. Parnianpour, "Predictive equations to estimate spinal loads in symmetric lifting tasks," *Journal of Biomechanics*, vol. 44, no. 1, pp. 84–91, Jan. 2011, ISSN: 00219290. DOI: 10.1016/j.jbiomech.2010.08.028.

[18] M. I. Mientjes, R. W. Norman, R. P. Wells, and S. M. McGill, "Assessment of an EMG-based method for continuous estimates of low back compression during asymmetrical occupational tasks.," *Ergonomics*, vol. 42, no. 6, pp. 868–79, Jun. 1999, ISSN: 0014-0139. DOI: 10.1080/001401399185342. [Online]. Available: http://www.ncbi.nlm.nih.gov/pubmed/10340027.

[19] A. Tabasi, M. Lazzaroni, N. P. Brouwer, *et al.*, "Optimizing Calibration Procedure to Train a Regression-Based Prediction Model of Actively Generated Lumbar Muscle Moments for Exoskeleton Control," *Sensors*, vol. 22, no. 1, p. 87, Dec. 2021, ISSN: 1424-8220. DOI: 10.3390/s22010087. [Online]. Available: https://www.mdpi.com/1424-8220/22/1/87.

[20] C. Pizzolato, D. G. Lloyd, M. Sartori, *et al.*, "CEINMS: A toolbox to investigate the influence of different neural control solutions on the prediction of muscle excitation and joint moments during dynamic motor tasks," *Journal of Biomechanics*, vol. 48, no. 14, pp. 3929–3936, Nov. 2015, ISSN: 18732380. DOI: 10.1016/j.jbiomech.2015.09.021.

[21] A. Moya-Esteban, G. Durandau, H. van der Kooij, and M. Sartori, "Real-time lumbosacral joint loading estimation in exoskeleton-

assisted lifting conditions via electromyography-driven musculoskeletal models," *Journal of Biomechanics*, vol. 157, Aug. 2023, ISSN: 18732380. DOI: 10.1016/j.jbiomech.2023.111727.

[22] R. Alberto, F. Draicchio, T. Varrecchia, A. Silvetti, and S. Iavicoli, "Wearable Monitoring Devices for Biomechanical Risk Assessment at Work: Current Status and Future Challenges-A Systematic Review.," *International journal of environmental research and public health*, vol. 15, no. 9, p. 2001, Sep. 2018, ISSN: 1660-4601. DOI: 10.3390/ijerph15092001. [Online]. Available: http://www.ncbi.nlm.nih.gov/pubmed/30217079%20http://www.pubmedcentral.nih.gov/articlerender.fcgi?artid=PMC6163390.

[23] M. I. Mohamed Refai, A. Moya-Esteban, and M. Sartori, "Electromyography-driven musculoskeletal models with time-varying fatigue dynamics improve lumbosacral joint moments during lifting," *Journal of Biomechanics*, vol. 164, p. 111 987, Feb. 2024, ISSN: 00219290. DOI: 10.1016/j.jbiomech.2024.111987. [Online]. Available: https://linkinghub.elsevier.com/retrieve/pii/S0021929024000642.

[24] D. Ao, M. S. Shourijeh, C. Patten, and B. J. Fregly, "Evaluation of Synergy Extrapolation for Predicting Unmeasured Muscle Excitations from Measured Muscle Synergies," *Frontiers in Computational Neuroscience*, vol. 14, Dec. 2020, ISSN: 1662-5188. DOI: 10.3389/fncom.2020.588943. [Online]. Available: https://www.frontiersin.org/articles/10.3389/fncom.2020.588943/full.

[25] D. Ao, M. M. Vega, M. S. Shourijeh, C. Patten, and B. J. Fregly, "EMG-driven musculoskeletal model calibration with estimation of unmeasured muscle excitations via synergy extrapolation," *Frontiers in Bioengineering and Biotechnology*, vol. 10, Sep. 2022, ISSN: 2296-4185. DOI: 10.3389/fbioe.2022.962959. [Online]. Available: https://www.frontiersin.org/articles/10.3389/fbioe.2022.962959/full.

[26] N. A. Bianco, C. Patten, and B. J. Fregly, "Can Measured Synergy Excitations Accurately Construct Unmeasured Muscle Excitations?" *Journal of Biomechanical Engineering*, vol. 140, no. 1, Jan. 2018, ISSN: 15288951. DOI: 10.1115/1.4038199.

[27] G. Averta, M. Iuculano, P. Salaris, and M. Bianchi, "Optimal Reconstruction of Human Motion From Scarce Multimodal Data," *IEEE Transactions on Human-Machine Systems*, vol. 52, no. 5, pp. 833–842, Oct. 2022, ISSN: 21682305. DOI: 10.1109/THMS.2022.3163184.

[28] P. Bonifati, M. Baracca, M. Menolotto, G. Averta, and M. Bianchi, "A Multi-Modal Under-Sensorized Wearable System for Optimal Kinematic and Muscular Tracking of Human Upper Limb Motion," *Sensors*, vol. 23, no. 7, p. 3716, Apr. 2023, ISSN: 1424-8220. DOI: 10.3390/s23073716. [Online]. Available: https://www.mdpi.com/1424-8220/23/7/3716.

[29] E. Bizzi, V. Cheung, A. d'Avella, P. Saltiel, and M. Tresch, "Combining modules for movement," *Brain Research Reviews*, vol. 57, no. 1, pp. 125–133, Jan. 2008, ISSN: 01650173. DOI: 10.1016/j.brainresrev.2007.08.004. [Online]. Available: https://linkinghub.elsevier.com/retrieve/pii/S0165017307001774.

[30] R. E. Singh, K. Iqbal, G. White, and T. E. Hutchinson, "A Systematic Review on Muscle Synergies: From Building Blocks of Motor Behavior to a Neurorehabilitation Tool," *Applied Bionics and Biomechanics*, vol. 2018, pp. 1–15, 2018, ISSN: 1176-2322. DOI: 10.1155/2018/3615368. [Online]. Available: https://www.hindawi.com/journals/abb/2018/3615368/.

[31] C. K. Tan, H. Kadone, K. Miura, *et al.*, "Muscle Synergies During Repetitive Stoop Lifting With a Bioelectrically-Controlled Lumbar Support Exoskeleton," *Frontiers in Human Neuroscience*, vol. 13, Apr. 2019, ISSN: 1662-5161. DOI: 10.3389/fnhum.2019.00142. [Online]. Available: https://www.frontiersin.org/article/10.3389/fnhum.2019.00142/full.

[32] E. Sedaghat-Nejad, S. J. Mousavi, M. Hadizadeh, *et al.*, "Is there a reliable and invariant set of muscle synergy during isometric biaxial trunk exertion in the sagittal and transverse planes by healthy subjects?" *Journal of biomechanics*, vol. 48, no. 12, pp. 3234–41, Sep. 2015, ISSN: 1873-2380. DOI: 10.1016/j.jbiomech.2015.06.032. [Online]. Available: http://www.ncbi.nlm.nih.gov/pubmed/26189578.

[33] W. Wang, N. Jiang, L. Teng, *et al.*, "Synergy Analysis of Back Muscle Activities in Patients With Adolescent Idiopathic Scoliosis Based on High-Density Electromyogram," *IEEE Transactions on Biomedical Engineering*, vol. 69, no. 6, pp. 2006–2017, Jun. 2022, ISSN: 0018-9294. DOI: 10.1109/TBME.2021.3133583. [Online]. Available: https://ieeexplore.ieee.org/document/9645180/.

[34] N. A. Turpin, S. Uriac, and G. Dalleau, "How to improve the muscle synergy analysis methodology?" *European Journal of Applied Physiology*, vol. 121, no. 4, pp. 1009–1025, Apr. 2021, ISSN: 1439-6319. DOI: 10.1007/s00421-021-04604-9. [Online]. Available: http://link.springer.com/10.1007/s00421-021-04604-9.

[35] S. Tahmid, J. M. Font-Llagunes, and J. Yang, "Upper Extremity Muscle Activation Pattern Prediction Through Synergy Extrapolation and Electromyography-Driven Modeling," *Journal of Biomechanical Engineering*, vol. 146, no. 1, Jan. 2024, ISSN: 0148-0731. DOI: 10.1115/1.4063899. [Online]. Available: https://asmedigitalcollection.asme.org/biomechanical/article/146/1/011005/1169823/Upper-Extremity-Muscle-Activation-Pattern.

[36] K. Manohar, B. W. Brunton, J. N. Kutz, and S. L. Brunton, "Data-Driven Sparse Sensor Placement for Reconstruction: Demonstrating the Benefits of Exploiting Known Patterns," *IEEE Control Systems*, vol. 38, no. 3, pp. 63–86, Jun. 2018, ISSN: 1066-033X. DOI: 10.1109/MCS.2018.2810460. [Online]. Available: https://ieeexplore.ieee.org/document/8361090/.

[37] Z.-C. Li, H.-T. Huang, J.-T. Chen, and Y. Wei, "Effective condition number and its applications," *Computing*, vol. 89, no. 1-2, pp. 87–112, Aug. 2010, ISSN: 0010-485X. DOI: 10.1007/s00607-010-0098-8. [Online]. Available: http://link.springer.com/10.1007/s00607-010-0098-8.

[38] C. G. Drury, C.-H. Law, and C. S. Pawenski, "A Survey of Industrial Box Handling," *Human Factors: The Journal of the Human Factors and Ergonomics Society*, vol. 24, no. 5, pp. 553–565, Oct. 1982, ISSN: 0018-7208. DOI: 10.1177/001872088202400505. [Online]. Available: http://journals.sagepub.com/doi/10.1177/001872088202400505.

[39] P. G. Dempsey, "A survey of lifting and lowering tasks," *International Journal of Industrial Ergonomics*, vol. 31, no. 1, pp. 11–16, Jan. 2003, ISSN: 01698141. DOI: 10.1016/S0169-8141(02)00104-X. [Online]. Available: https://linkinghub.elsevier.com/retrieve/pii/S016981410200104X.

[40] S. M. Mcgill, "Electromyographic Activity of the Abdominal and Low Back Musculature During the Generation of Isometric and Dynamic Axial Trunk Torque: Implications for Lumbar Mechanics," Tech. Rep., 1991, pp. 991–103.

[41] F. J. Vera-Garcia, J. M. Moreside, and S. M. McGill, "MVC techniques to normalize trunk muscle EMG in healthy women," *Journal of Electromyography and Kinesiology*, vol. 20, no. 1, pp. 10–16, Feb. 2010, ISSN: 10506411. DOI: 10.1016/j.jelekin.2009.03.010.

[42] J. H. van Dieën and I. Kingma, "Effects of antagonistic co-contraction on differences between electromyography based and optimization based estimates of spinal forces.," *Ergonomics*, vol. 48, no. 4, pp. 411–26, Mar. 2005, ISSN: 0014-0139. DOI: 10.1080/00140130512331332918. [Online]. Available: http://www.ncbi.nlm.nih.gov/pubmed/15804849.

[43] E. Beaucage-Gauvreau, W. S. Robertson, S. C. Brandon, *et al.*, "Validation of an OpenSim full-body model with detailed lumbar spine for estimating lower lumbar spine loads during symmetric and asymmetric lifting tasks," *Computer Methods in Biomechanics and Biomedical Engineering*, vol. 22, no. 5, pp. 451–464, Apr. 2019, ISSN: 14768259. DOI: 10.1080/10255842.2018.1564819.

[44] I. Kingma, G. S. Faber, and J. H. van Dieën, "Supporting the upper body with the hand on the thigh reduces back loading during lifting," *Journal of Biomechanics*, vol. 49, no. 6, pp. 881–889, Apr. 2016, ISSN: 00219290. DOI: 10.1016/j.jbiomech.2015.09.035. [Online]. Available: https://linkinghub.elsevier.com/retrieve/pii/S0021929015005308.

VI. APPENDIX

A. Marker Placement

Figure 10 shows the markers listed in table VIII.

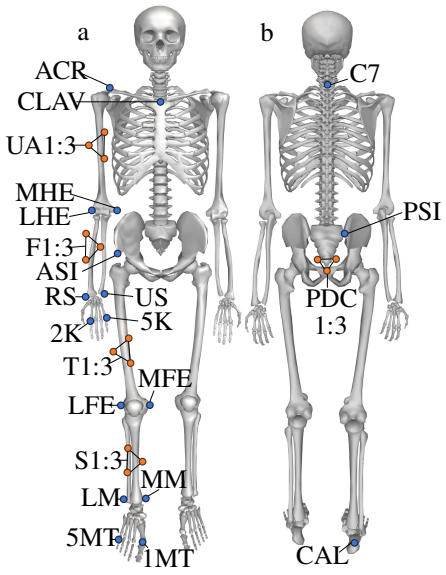

Fig. 10. Placement of the spherical reflective markers from anterior (a) and posterior (b). Blue markers indicate placement on bony landmarks, and orange markers indicate triplet clusters.

TABLE VIII
OVERVIEW OF ALL BODY MARKERS.

Body Set	Abbreviation	Location	Number of markers (Left and Right)	Marker type
Torso	CLAV	Clavicle	1	Bony
	ACR	Acromion	2	Bony
	C7	Vertebra C7	1	Bony
Humerus	UA1:3	Upper arm cluster	6	Cluster
	MHE	Medial humeral epicondyle	2	Bony
	LHE	Lateral humeral epicondyle	2	Bony
Radius	F1:3	Forearm cluster	6	Cluster
	RS	Radial styloid	2	Bony
Ulna	US	Ulnar syloid	2	Bony
Hand	1K	First knuckle (metacarpophalangeal joint)	2	Bony
	5K	Fifth knuckle (metacarpophalangeal joint)	2	Bony
Pelvis	ASI	Anterior superior iliac spine	2	Bony
	PSI	Pelvic sacro iliac joint	2	Bony
	PDC1:3	Pelvis dorsal cluster (attached to a wrap around the pelvis)	3	Cluster
Femur	T1:3	Thigh cluster	6	Cluster
	MFE	Medial femoral epicondyle	2	Bony
	LFE	Lateral femoral epicondyle	2	Bony
Tibia	S1:3	Shin cluster	6	Cluster
	MM	Medial malleolus	2	Bony
	LM	Lateral malleolus	2	Bony
Calcaneus	1MT	First metatarsal	2	Bony
	5MT	Fifth metatarsal	2	Bony
	CAL	Calcaneus	2	Bony
		$\sum_{markers}$	61	

B. *Inverse synergy-based method - MATLAB code*

Listing 1 shows the MATLAB code for the inverse synergy-based method. The number of synergies k comes from synergy extraction from calibration data (see section III-F.2). The number of sensors is a free parameter and should be at least equal to k. If the number of sensors exceeds k, the placement is oversampled (see section II-C).

Listing 1. Matlab code of the inverse synergy-based method

```
k = 2; nrSensors = k;   % Free parameters,
load('TrainingData.V')  % m x n EMG envelopes
load('Testdata.V')      % m x n EMG envelopes

%%%%% Calibration - use only Training data %%%%%
% Grid search
opt = statset('MaxIter',100,'Display','off');
[NNMF.W0,NNMF.H0] = nnmf(TrainingData.V,k,'Replicates',150, 'Options', opt, 'Algorithm','mult');
% Local search
opt = statset('Maxiter',300,'Display','off');
[NMF.W,NMF.H] = nnmf(TrainingData.V,k,'W0',NNMF.W0, 'H0',NNMF.H0, 'Options',opt, 'Algorithm','als');

% Find optimal sensor order
if (nrSensors == k)
[¬,¬,pivot] = qr(NMF.W','vector');
elseif (nrSensors > k)                      % Oversampled QR sensors
[¬,¬,pivot] = qr(NMF.W*NMF.W','vector');
end

% Select k optimal sensors
sensors = pivot(1:nrSensors);

%%%%% Execution - use only Test data %%%%%
% Select only measured EMG channels
EMGmeas(1:nrSensors,:) = TestData.V(sensors,:);

% Obtain reconstructed H (H*)
reconH = NMF.W(sensors,:)\EMGmeas;

% Obtain reconstructed EMG
EMGest = (NMF.W*reconH);
```

C. Analysis of synergy vectors and sensor location

Figure 11 shows how the optimal sensor placement is related to the synergy vector matrices (**W**) of all participants.

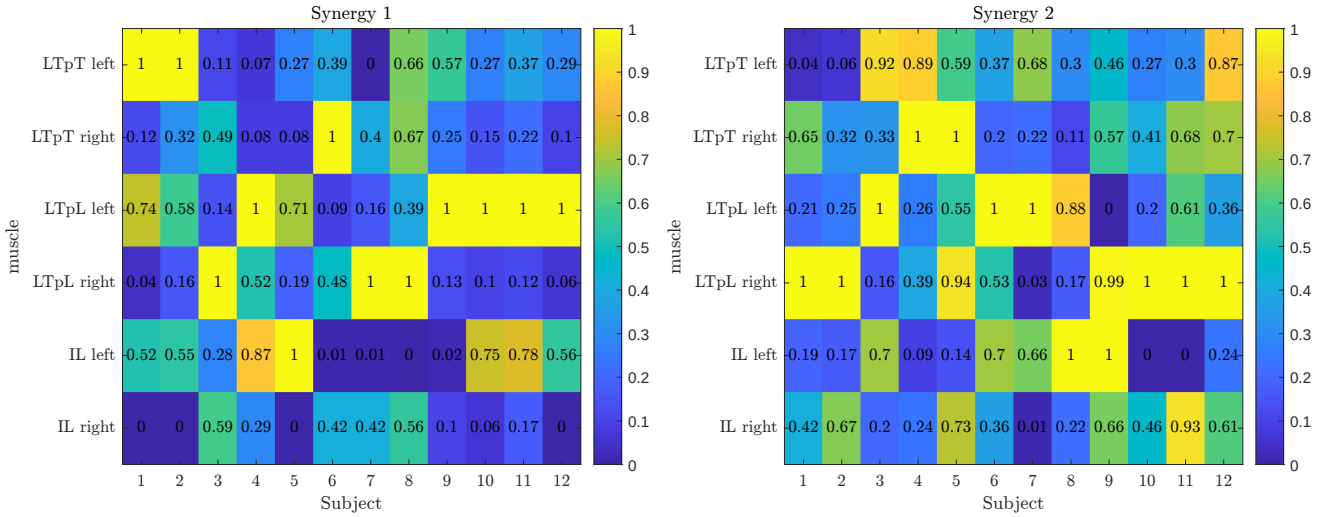

(a) (b)

Fig. 11. Combined overview of the relative synergy vector matrices **W** for each subject. The values are scaled relatively to the maximum value (1) which also indicates the optimal sensor location for that specific synergy. So for example, subject 1 has the LTpT left muscle for synergy 1 as optimal sensor location, and for synergy 2 the LTpL right. The relative $\mathbf{W}_{(6\times2)}$ for each subject can be found by combining the columns of the corresponding subject for synergy 1 and 2. We observe that all subjects had bilateral sensor placement, except subject 9, who had two left-sided optimal sensors (LTpL left and IL left). We noted that for subject 9 the value of synergy 2 for LTpL right is very close to 1 (0.99). Explanation of these findings requires further evaluation.

D. Reconstruction accuracy of EMG with passive exoskeleton

Additional data was collected from all 12 participants while wearing a Laevo Flex passive exoskeleton. The exoskeleton was individually fitted to each participant based on manufacturer specifications and user comfort. A medium stiff gas spring (42 kN/m) was uniformly used across all participants (for detailed specifications, see [21]). Data was collected for all lifting techniques (SQ, ST, UT, BT) with a 15 kg box weight only. The number of repetitions was similar (six repetitions for SQ and ST, three repetitions for UT and BT) Table IX shows median RMSE and R^2 values. Median RMSE values ranged between 0.03 and 0.05 relative to MVC, while median R^2 values ranged between 0.74 and 0.79. To assess the impact of exoskeleton usage on EMG reconstruction accuracy, results from Table IX were compared to those from Table V for the 15 kg techniques. RMSE values remained similar, whereas R^2 values slightly decreased in exoskeleton trials. The implications of these differences on lumbosacral joint moments and compression forces remain unclear, as no dynamics model was used to quantify the exoskeleton's assistance on the body. Including this model enables a comparison of lumbosacral joint moments and compression forces between full- and reduced-EMS. This allows for an evaluation of the continued validity of the calibrated $\mathbf{W}^*$ and optimal sensor locations from the inverse synergy-based approach when wearing a passive exoskeleton.

TABLE IX

RMSE AND R^2 BETWEEN REFERENCE EMG ($\mathbf{V}_{val}$) AND RECONSTRUCTED EMG ($\mathbf{V}_{rec}$) WHILE WEARING A PASSIVE LAEVO FLEX EXOSKELETON. MEDIAN VALUES (IQR) ACROSS ALL PARTICIPANTS ARE SHOWN.

	EMG*	
	RMSE [-]	R^2 [-]
SQ 15 kg	0.04 (0.02)	0.74 (0.30)
ST 15 kg	0.05 (0.03)	0.74 (0.26)
UT 15 kg	0.03 (0.02)	0.79 (0.29)
BT 15 kg	0.04 (0.02)	0.77 (0.33)

*Reconstructed sensors only